

Data-driven Radiative Magnetohydrodynamics Simulations with the MURaM Code: the Emergence of Active Region 11158 and the X2.2 Flare

FENG CHEN ^{1,2}

¹*School of Astronomy and Space Science, Nanjing University, Nanjing 210023, China*

²*Key Laboratory of Modern Astronomy and Astrophysics (Nanjing University), Ministry of Education, Nanjing 210023, China*

ABSTRACT

We present the application of the data-driven branch of the MURaM code to the extensively studied flare-productive active region 11158. We refine the hybrid model strategy, which was described in the earlier paper of this series, to model the emergence of the active region during 4 solar days starting shortly before 2011 February 11 and the eruption of an X2.2 flare on February 15. After 4 days of evolution, a major eruption of a magnetic flux rope occurs in the simulation at approximately 3 hours (3% difference) before the real flare. The eruption leads to magnetic reconnection that contributes to bulk heating in the chromosphere and corona. The deposition of flare energy in the chromosphere causes strong condensations and evaporations, which fill hot post-flare loops and bright flare ribbons that exhibit separation and extension similar to the observed ribbon evolution. The synthesized soft X-ray flux corresponds to X class, which is close to the real event. The upward eruption of the flux rope leads to a piston-driven shock and horizontal expansion that exerts a strong downward impact on the lower atmosphere and generate an apparently fast-propagating chromospheric Moreton wave. We conclude that the data-driven radiative simulation of this active region can reproduce the key observational results of the real flare and demonstrate the great potential of this method for studying solar eruptions in a realistic corona environment.

Keywords: Radiative magnetohydrodynamics (2009), Magnetohydrodynamical simulations(1966), Solar magnetic flux emergence (2000), Solar magnetic reconnection(1504), Solar active regions(1974), Solar flares(1496), Solar coronal mass ejections(310)

1. INTRODUCTION

Solar eruptions represent perhaps the most complex and dynamic interaction between solar magnetic field and plasma. The community has recognized the important application of numerical simulations that follow the observed evolution of photospheric magnetic fields and consider sophisticated physical processes for realistic plasma properties.(Patsourakos et al. 2020; Jiang et al. 2022; Guo et al. 2024; Jiang 2024; Schmieder et al. 2024)

Following previous papers in this series that described the implementation of the data-driven boundary in the Radiative MHD code MURaM (Chen et al. 2023a) and the application on non-eruptive emerging an active region (Chen 2025), we apply this method to a well-known and extensively studied active region 11158, which pro-

duced the first X class flare in solar cycle 24 (Schrijver et al. 2011) and has been thoroughly analyzed from its emission properties (e.g., Young et al. 2013; Milligan et al. 2014) to magnetic structures (e.g., Liu & Schuck 2012; Sun et al. 2012; Wang et al. 2012; Vemareddy et al. 2012; Tziotziou et al. 2013; Kazachenko et al. 2015; Sun et al. 2017).

In particular, data-driven magnetohydrodynamic (MHD) simulations under different approximations have been employed to investigate the evolution and eruptions in this active region. Cheung & DeRosa (2012) and Lumme et al. (2017) conducted a magneto-frictional calculation to model the evolution of the coronal magnetic field over several days of emergence. These models omit the role of plasmas and represent a progress of methodology from a series of static magnetic field calculations (Jarolim et al. 2023) to a full MHD simulation that includes both magnetic fields and plasmas.

Inoue et al. (2014, 2015) used a nonlinear-forcefree-field as the initial condition for an MHD simulation and

modeled the magnetic evolution of during the X class flare, and Inoue et al. (2018) investigated the M6.6 flare that occurred two days earlier. Hayashi et al. (2018, 2019) conducted MHD simulations for approximately 15 hours with a focus on testing different methods of driving the boundary and the accumulation of magnetic energy in the coronal volume.

Recently, MHD simulations with improved treatments for the plasma thermodynamics have become possible. The hybrid model of Afanasyev et al. (2023) covers the emergence of the magnetic field via a magneto-friction calculation and the eruption via an MHD simulation with thermal conduction and almost isothermal equation of state. Fan et al. (2024) improved the energy equation by including the missing radiative loss and more self-consistent heating to maintain the corona temperature. Their model setup has a sufficient spatial extent, which allows investigations of the large-scale impact of the eruption, such as coronal extreme-ultraviolet (EUV) waves. A global scale model of the X class flare in AR 11158 was reported by Jin et al. (2022), who investigated the large-scale dimming associated with coronal mass ejection (CME). Hoeksema et al. (2020) (and references therein) presented a comprehensive test of the capability of driving local/global scale magneto-frictional models and radiative MHD models that reproduced the pre-eruption state of AR 11158.

The well-studied AR 11158 serves as an ideal example of testing and validating the data-driven branch of the MURaM code, which may provide new insight complementing the detailed studies that have been performed. This work is a part of a comprehensive project of an international collaboration to model evolving and erupting active regions. As the first attempt, we prefer to use a simple setup following Cheung & DeRosa (2012) to drive the evolution, which is sufficient to capture the most important magnetic structure for the eruption. The comprehensive model describes, at the same time, the eruption at the large-scale corona, as well as the detailed plasma dynamics in different layers of the atmosphere, which, to the best of our knowledge, has not been done in previous works. The rest of the paper is organized as follows. We described in Section 2 the multi-stage model strategy and setup of the numerical simulations. The results are presented in Section 3, and a summary and discussion are given in Section 4.

2. METHODS

We follow the method presented in our previous papers Chen et al. (2023a) and Chen (2025) to implement the data-driven bottom boundary and to conduct multi-stage simulations. Here, we describe the particular mod-

ification of the method and model setup for this active region.

2.1. The Data-Driven Boundary

The horizontal electric field $\mathbf{E}_h = (E_x, E_y)$ that is needed to drive the induction equation is solved from

$$\nabla \times \mathbf{E}_h = -\frac{\Delta B_z}{\Delta t} \quad (1)$$

$$\nabla \cdot \mathbf{E}_h = -\Omega B_z, \quad (2)$$

where B_z is the radial component of the vector magnetic field observed by SDO/HMI (Scherrer et al. 2012; Hoeksema et al. 2014), $\Delta t = 720$ s the cadence of the observations, and $\Omega = 1.0 \times 10^{-5} \text{ s}^{-1}$. Ω represents a rotation applied on a vertical flux tube and is the primary parameter that controls the injection of free magnetic energy into the domain, as described in earlier papers (Cheung & DeRosa 2012; Chen 2025). We use an educated guess on the basis of the relative motion of the flux concentrations in this active region.

The evolution of the vertical magnetic field in the photosphere is shown in the top row of Figure 1. This active region, as marked in Figure 1, comprises of two major sunspot pairs, P1–N1 and P2–N2³, and a small parasitic bipole, P3–N3 (N3 merges with N2 and is not marked in the figure), that emerges after February 14, next to the northern edge of the N2 spot. The P3 flux concentration continues to intrude into the area surrounded by the N1, P2, and N2 spots, which causes the destruction of a pre-existing flux rope at the onset of the eruption, as demonstrated later in this paper. The relative shearing and collisional motion between two large sunspot pairs, particularly between N1 and P2, creates a strongly sheared polarity inversion line (PIL) and is suggested to be the key process for generating free magnetic energy in the corona (Toriumi et al. 2017; Chintzoglou et al. 2019; Rempel et al. 2023). We estimate the order of magnitude of Ω from the sunspot motion as follows. The shearing motion is treated as an equivalence of the N1 spot rotating around the P2 spot. In two days, N1 rotated by approximately $\pi/2$ rad with respect to P2, according to a comparison of Panels (b) and (d) in Figure 1 (see also Figure 3 in Sun et al. 2012), which corresponds to a rotation period of 8 days. In the case of solid body rotation, the vorticity of $1.0 \times 10^{-5} \text{ s}^{-1}$ corresponds to a period of 14.6 days. Control experiments with $\Omega = 0$ or $6 \times 10^{-6} \text{ s}^{-1}$ yield no major eruptions by the end of February 15.

³ Sun et al. (2012) denoted them as P0–N0 and P1–N1.

2.2. A Three-Stages Hybrid Strategy

We modify the two-stage hybrid strategy described in [Chen \(2025\)](#) to address the combined evolution of the emergence of AR 11158, the formation of coronal plasma structures, and the onset and propagation of the eruption.

2.2.1. Zero- β Model

The computational domain of a zero- β simulation is resolved by $256 \times 256 \times 1152$ grid points. The grid spacing are 576 km and 64 km in the horizontal and vertical directions, respectively. This setup represents a horizontal domain that is smaller than the actual active region by a factor of 1.875. As in the zero- β run in [Chen \(2025\)](#), a speed up factor $f_{sp} = 12$ is applied to the time series of the observed magnetic field such that the interval of consecutive magnetograms becomes 60 s. The simulation starts from February 10, 22^h UT and is evolved for approximately 6×10^5 iterations, which covers an equivalent time period of almost 5 days. As shown in Section 3, a strong decay in the magnetic energy is detected at the equivalent time of approximately February 15, 0^h UT. The properties of the eruption need to be modeled via sophisticated MHD simulations.

2.2.2. Radiative MHD Model for the Corona

The second stage is a radiative MHD run (hereafter, *evo. run*) that models the coronal plasma before the eruption of interest. The speed up factor of time is NOT applied in the MHD simulations. The MHD run is started from approximately February 14, 20^h UT on the basis of a zero- β run snapshot.

A major modification to the method described in [Chen \(2025\)](#) is that the MHD model represents the one-to-one size of the actual active region. The simulation domain is resolved by a $512 \times 512 \times 1920$ mesh, with a horizontal/vertical grid spacing of 540 km/64 km. This setup leads to a domain width of 276.48 Mm and a height of 122.88 Mm. To construct the initial magnetic field, we calculate a potential field \mathbf{B}^P from the observed vertical magnetic field, with a periodic side boundary and the assumption of a vanishing field at infinity. It is convenient to calculate the non-potential field \mathbf{B}^{NP-256} from the zero- β snapshot. The coordinates of this cube in all three direction are scaled up by a factor of 1.875 to match the size of the actual active region, and \mathbf{B}^{NP} is obtained by interpolating the non-potential field cube to the mesh of the MHD run. Finally the initial magnetic field is constructed by

$$\mathbf{B}^{\text{init}} = \mathbf{B}^P + \mathbf{B}^{NP} + \mathbf{B}^{\text{QS}}, \quad (3)$$

where \mathbf{B}^{QS} is the magnetic field adapted from a fully relaxed quiet Sun simulation similar to that shown in [Chen et al. \(2022\)](#).

The initial plasma conditions are also adapted from the quiet Sun simulation. As we found in simulations for a non-erupting active region ([Chen 2025](#)), the active region corona evolves on the basis of the heating in the coronal volume and is almost independent of the initial plasma conditions.

The MHD model is evolved until the expected eruption of interest occurs, which takes approximately 3.2 hours. We set up a new MHD model with a further extend vertical domain to model the dynamics of the eruption.

2.2.3. Radiative MHD Model for the Eruption

The third stage in the hybrid model is an MHD simulation with an extend vertical domain (hereafter, *flare run*). The flare run has a mesh of $512 \times 512 \times 3840$ grid points with the same grid spacing as the *evo. run*; thus, the domain height is extended to 245.76 Mm.

The flare run is initiated from the snapshot of the *evo. run* at 300000 iterations, corresponding to February 14, 23^h5^m. The lower 1920 grid points of the initial condition are copied from the *evo. run* snapshot. The magnetic field in the upper 1920 grid points is a potential field calculated from the vertical magnetic field in the top $x - y$ plane of the *evo. run* snapshot. The density and internal energy in the upper 1920 grid points are uniform in the horizontal direction and are extrapolated in height following the mean gradient of the uppermost 10 Mm in the *evo. run*. This yields a stratification that is very close to hydrostatic equilibrium. The initial velocity in the upper half of the flare run domain vanishes.

3. RESULTS

3.1. Emergence of the Active Region and Energy Budget of the Eruption

The coronal magnetic field in the zero- β run across 4 days⁴ are displayed in Panels (e) – (h) of Figure 1. The seed points for calculating fieldlines are uniformly distributed in the rectangular area covering the sunspots in this active region. In the latter two days, the coronal fieldlines closely resemble the shape of observed EUV loops. However, a quantitative investigation of the formation of these loops requires a model with much finer

⁴ The first three columns show the snapshots corresponding to about 0^h UT of each day, whereas the last column shows the snapshot corresponding to February 14, 20^h UT, which is identical to the initial state of the MHD *evo. simulation*.

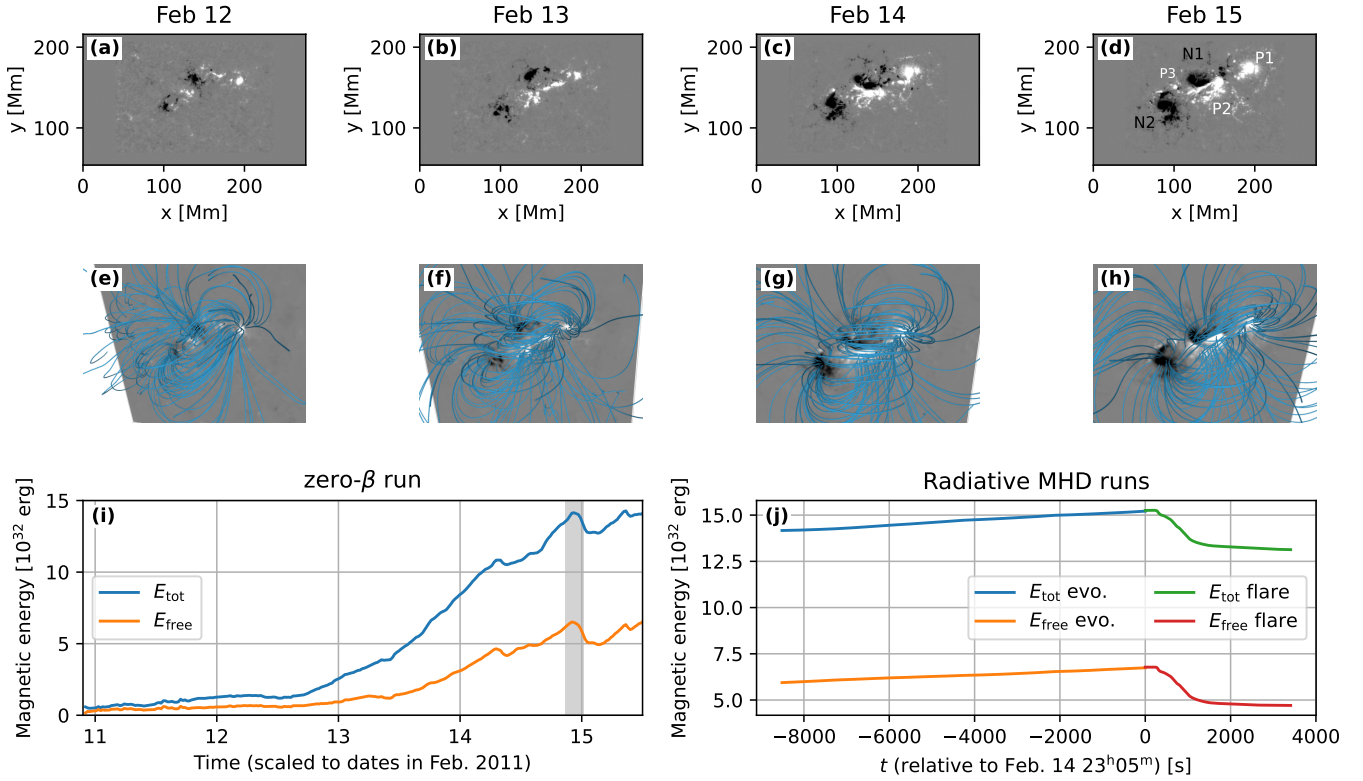


Figure 1. The upper panels display the evolution of the observed radial magnetic field of AR 11158. The second row illustrates the coronal magnetic field in the zero- β run. Fieldlines are calculated from static seed points that are uniformly distributed in a rectangular area covering the sunspots in the active region. The points of view are chosen according to the location of the real active region on the solar disk. The bottom row shows the evolution of the magnetic energy in the 4 days covered by the zero- β run and the rapid decay of the magnetic energy in the radiative MHD runs during the eruption, as indicated by the gray banner.

resolution, as suggested in our earlier study on a non-eruptive active region (Chen 2025).

A crucial parameter of flare-productive active regions is the free magnetic energy stored in the corona. Panel (i) of Figure 1 plots the evolution of volume-integrated total magnetic energy E_{tot} and free magnetic energy E_{free} in the zero- β run⁵. The rapid increase in the magnetic energy starts from February 13, similar to the trend found in observations (Sun et al. 2012). In our model, the magnetic energy increases to approximately 1.4×10^{33} erg with a very steady rate until a time corresponding to February 14, 23^h UT; meanwhile, the free magnetic energy accumulates to approximately 6.5×10^{32} erg. We note that this energy includes a large contribution from the curved/twist magnetic field outside the core region of the domain, which is an effect of the constant Ω and periodic side boundary. An abrupt

decay in the free magnetic energy, as indicated by the gray mask in Panel (i), indicates a major eruption, which occurs approximately 3 hours earlier than the actual X2.2 flare on real Sun.

The self-consistent evolution of the plasma and magnetic fields from development to eruption is described by the evo. and flare runs. Figure 1(j) shows the joint evolution of the total and free magnetic energy since 2.5 hours before the flare onset. The time t hereafter are relative to the beginning of the MHD flare run. The free magnetic energy steadily increases and starts to decrease at $t = 219$ s. The fast decay lasts for approximately 1000 s, during which 1.94×10^{32} erg magnetic energy is released.

3.2. Magnetic Structure and Plasma Dynamics of the Eruption

We present in this section the eruption of a flux rope and the large-scale dynamics in the model atmosphere.

3.2.1. Slow Rise and Fast Eruption of the Flux Rope

We use density structures to trace the kinematic evolution of the flux rope, as in our previous studies (Wang

⁵ On the basis of the setup of the zero- β run, the magnetic energy and time are multiplied by a factor of 1.875³ and 12, respectively, such that they can be directly compared with quantities of the MHD simulations

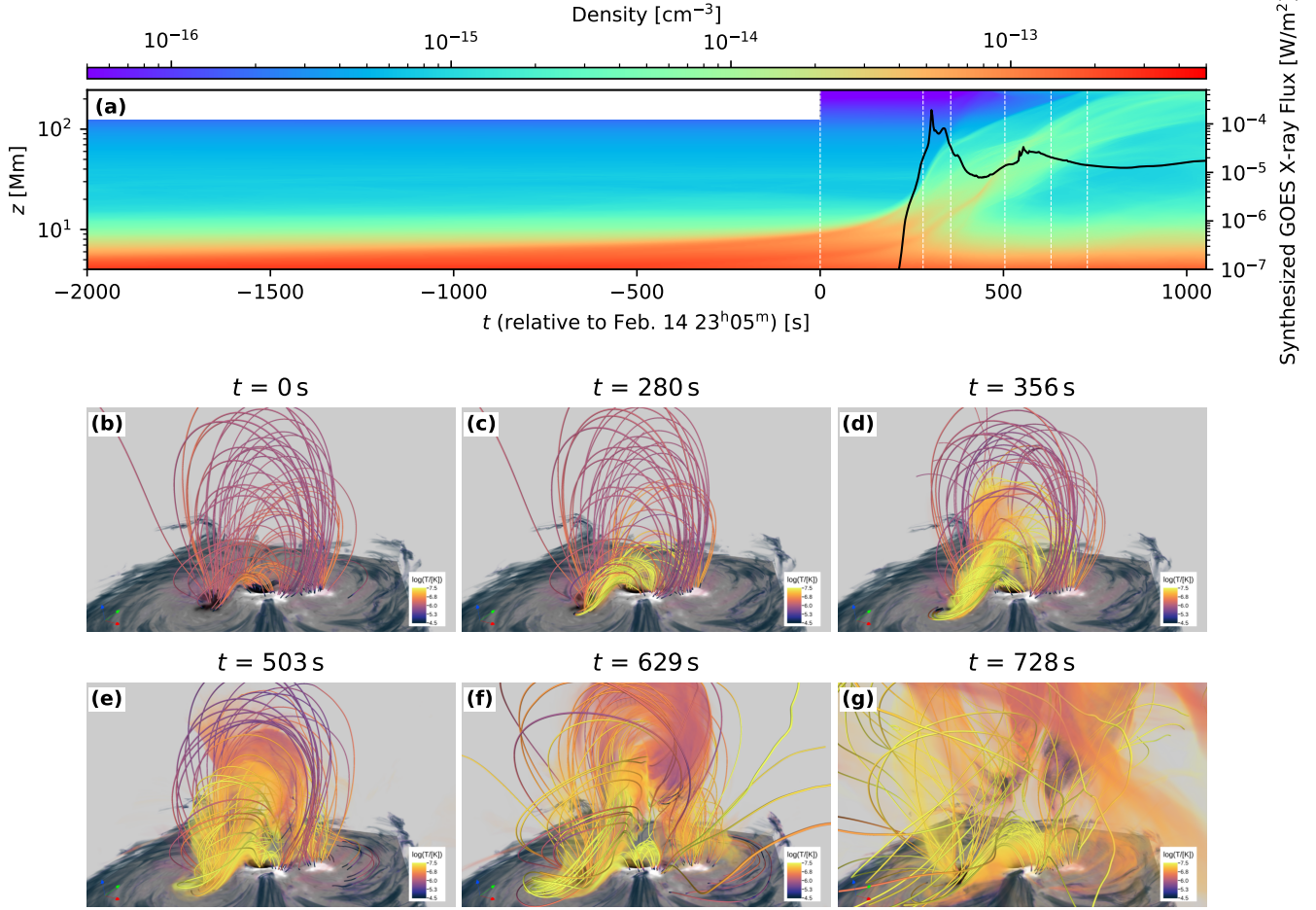


Figure 2. Course of the eruption. Panel (a) shows the horizontally averaged density from the combined data of the evo. and flare runs, which illustrate the slow rise and eruption of a plasma-hosting magnetic flux rope. The overlay black line plots the synthesized GOES 1-8Å soft X-ray flux, which indicates a flare above X class. Panels (b)–(g) present 3D visualizations of the plasma and magnetic field structures of the eruption. The corresponding time stamps are marked by the white dashed lines in Panel (a). The opacity of the features is chosen on the basis of the plasma density in the erupted flux rope, whereas lower and higher values are made transparent. The magnetic field lines are calculated from seed points that are randomly distributed in the coronal volume above the sunspots. The color of the density features and fieldlines reflects the plasma temperature on a logarithmic scale.

et al. 2023) and in observations where ejected plasma is tracked (Cheng et al. 2020, and reference therein). Figure 2(a) presents the horizontally averaged plasma density as a function of time. The 3000 s time period covers the slow rise of the flux rope before the rapid eruption. The height z starting from 4 Mm is displayed on a logarithmic scale to highlight the lower part of the domain.

We calculate the soft X-ray flux with a temperature response function of the GOES-15 satellite, which is overlaid on the density profile. The peak flux of $1.97 \times 10^{-4} \text{ W m}^{-2}$ is found at $t \approx 300 \text{ s}$, which corresponds to an X2 class flare. The similarity in the soft X-ray flux is very likely only a *coincidence*, because real flares undergo physical processes, e.g., those related to

nonthermal particles (Aschwanden et al. 2016; Warmuth & Mann 2016), that are beyond the capability of the current numerical model. Therefore, the actual value of the soft X-ray flux is only compared with other simulations under similar approximations and is considered as an indicator of the strength of energy release and plasma heating. This flare is thus far the largest event, compared with early MURaM simulations in the literatures that produced flares corresponding to lower M (Chen et al. 2023b; Rempel et al. 2023) or C class (Cheung et al. 2019), with magnetic energy release on the order of 10^{31} erg .

For more 1000 s before the eruption, the flux rope steadily rises at a very small speed of approximately 2 km/s and progresses to rapid eruption around $t = 250 \text{ s}$

during the impulsive phase of the flare. The lead edge in the density profile is a piston-driven shock (presented later with more details). The main body of the flux rope rises at an average speed on the order of 200 km/s. Although the domain height is the maximum that our computational resources can afford, the shock and ejected plasma reaches the top boundary at approximately $t = 420$ s and $t = 700$ s, respectively. The top boundary is open for outflows but may still affect the upward propagation of the CME. Observations (e.g., Figure 9 in Schrijver et al. 2011) found a radial expansion front between 40–100 Mm above the surface with a deduce speed of 300 km/s at 4 min after the onset, which is similar to the propagation in this simulation.

3.2.2. Large-scale Magnetic Structure in the Eruption

We briefly present the magnetic and plasma structures in the early stage of the eruption in Panels (b) – (g) of Figure 2. Before eruption, the flux rope can be found along the PIL between N1 and P2 and is accompanied by sheared arcades on both sides. Cool plasma is hosted in the dip formed by a twisted magnetic field. Panel (c) shows the snapshot in the impulsive phase of the flare, during which reconnections occur between the pre-existing flux rope with ambient arcades and gives rise to 10 MK plasma in the core area between N1 and P2, which is the location of observed X-ray sources Zharkov et al. (2011); Wang et al. (2012). Panel (d) displays a snapshot shortly after the flare peak. The two hot arcades connecting to from the inner spots N1 and P2 to the outer spots P1 and N2, respectively, now reconnect to form a long sigmoid, which is considered as a new large flux rope that roots in P1 and N2, and at the same moment, post-flare loops connecting N2 and P1 are formed below the reconnection site.

The snapshots in the gradual phase are presented in Panels (e) – (g) of Figure 2. The long sigmoid continues to rise and push the plasma upward with ongoing reconnection below, which is similar to the mechanism found in more generalized numerical experiments (Jiang et al. 2021). New post-flare loops continue to form left (solar east or lower x) to right (solar west or higher x). The propagation of reconnection is supposed to drive the extension of flare ribbons, which is discussed later in this paper. Panel (g) illustrates the reconnection between the envelope field on the two sides of the erupted flux rope and the formation of longer and higher post-flare loops that are filled with plasma over 10 MK.

3.2.3. Plasma Dynamics in the Large-scale Corona

We analyze the emission measured weighted velocity v_{LOS} , which represents the Doppler velocity of a spectral line forming in the given temperature range, as done in

our previous studies (Chen et al. 2023a; Chen 2025). Figure 3 presents v_{LOS} in three temperature ranges that capture the chromosphere and transition region plasma, warm coronal plasma of million K, and hottest plasma around and above 10 MK.

The first row of Figure 3 shows a snapshot shortly after the peak of the flare. The low-temperature Doppler map reveals a strong downflow up to 100 km/s at the left end of the PIL between N2 and P1. The two ribbons of downflow outline the footpoints of the post-flare loops formed beneath the reconnection site, as illustrated in Figure 2 (d). The upflows embracing the downflow indicate fast ejection of chromosphere plasma. The upflow pattern, particularly the one above P3 in the intruding bipole, can be observed at all temperatures with increasing speed to over 1000 km/s in the hottest bins.

The second row displays Doppler maps in the gradual phase of the flare. The downflow ribbons significantly extend along the PIL, as we expected from the development of magnetic reconnection as shown in Figure 3(e) and (f). Moreover, the eruption produces more spatially extensive upflows of a few hundred km/s. Fan et al. (2024) reported a significant fieldline expansion at similar locations, which may explain the dimming observed during this eruption (Dissauer et al. 2018).

The bottom row presents a snapshot when the atmosphere is recovering from the highly dynamic state caused by the eruption. The time scale might not be realistic because the real eruption impacts a much larger volume than the domain size of the simulation and lasts significantly longer. Nevertheless, we see that, during this stage, the plasma velocities at all temperatures decrease to their typical values during a quiescent period.

Last but not least, the upward eruption of the magnetic structure during the impulsive and peak phases of the flare is accompanied by strong horizontal expansion as well, which eventually leads to a downward push at the outer rim of the active region, as shown by the increasing and sharpening downflow rims in Panels (b) and (e) of Figure 3. This gives rise to an intriguing interactions between different layers of the atmosphere as presented in detail in the following section.

3.3. CME Driven Shock and the Chromospheric Moreton Wave

We present in Figure 4 (a) the vertical velocity v_z near the peak of the flare, which is the identical snapshot as Figure 2 (d) and the top row of Figure 3 in a $y - z$ plane that cuts through the core region of the eruption. The plasma after the piston-driven shock has an upward velocity of 500 km/s, in contrast to the mild 200 km/s downward velocity in the background.

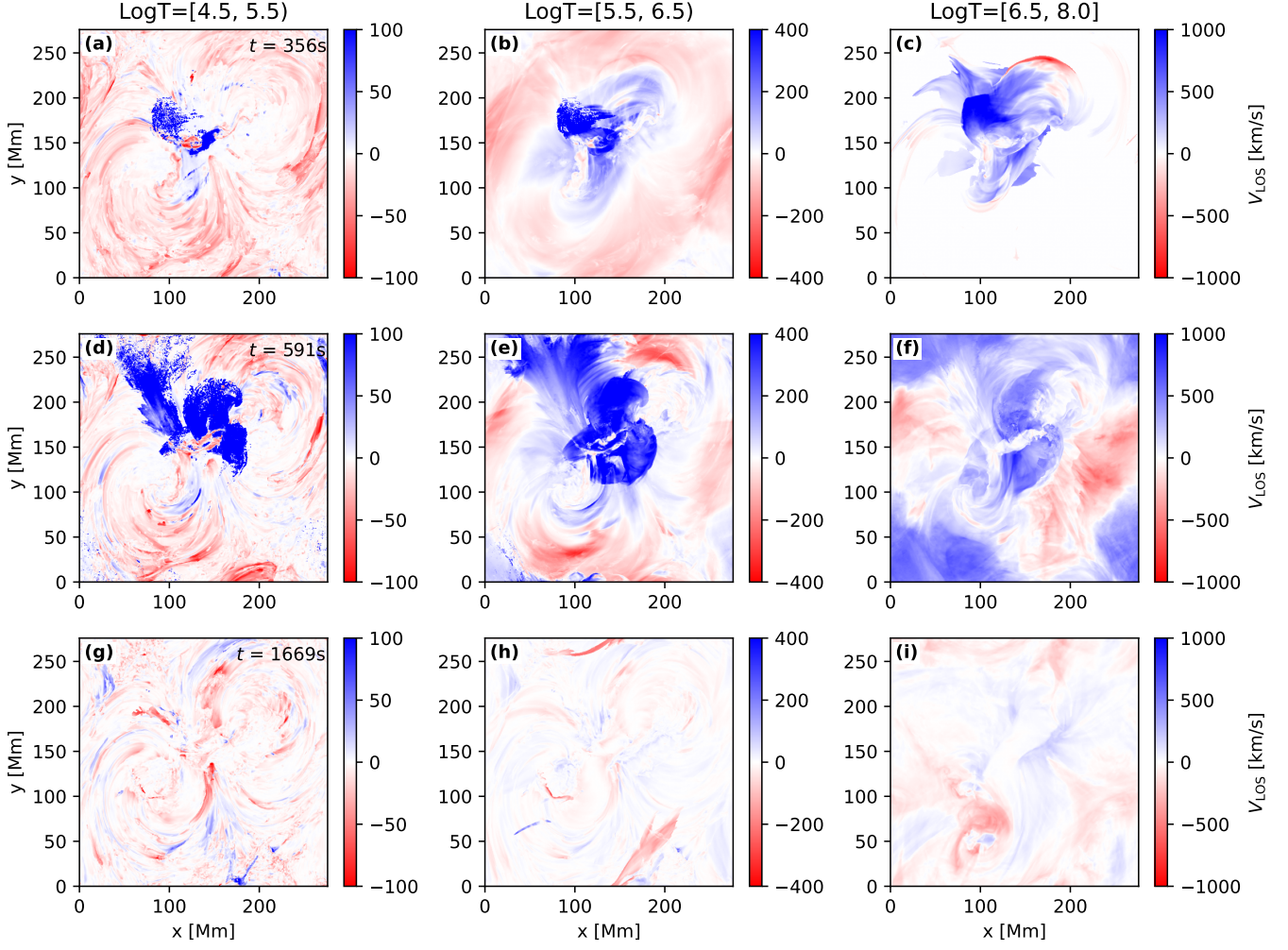


Figure 3. The emission measured line-of-sight velocity from a top view. It represents the Doppler velocity from a spectroscopic observation of an active region near the solar disk center. The original outputs of the emission measures and line-of-sight velocities at an interval of $\log T = 0.1$ are binned to three temperature ranges, as indicated at the top panel of each column, and the rows correspond to three snapshots as marked in the first panel of each row.

In comparison, Afanasyev et al. (2023) and Fan et al. (2024) reported velocities above or close to 1000 km/s after the shock front. The highest speed in this vertical slice is found immediately above the reconnection site at $z \approx 20$ Mm, which is up to 1500 km/s and accompanied by a 500 km/s downflow right below, which appears as a red point in Figure 4 (a).

Panels (b) and (c) display two time-distance diagrams of v_z along a vertical and a horizontal slit that are placed at locations indicated by the two dashed lines in Figure 4 (a), respectively. Panel (b) shows that the upward propagating disturbance is set off in the impulsive phase at approximately $t = 270$ s. The velocity gradient increases and develops into a shock (when it is resolved by 5 grid points in the vertical direction) at $t \approx 320$ s and $z \approx 170$ Mm. Afterward, the shock propagates at a rather constant speed of approximately 1000 km/s.

Moreover, Figure 4 (b) shows similar branches, as illustrated in Figure 2 (a), where we see a fast propagating shock front and a flux rope that rise at a small speed.

The diagram in Figure 4 (c) aims to capture the impact of the eruption at the outer part of the active region. We find numerous thin ridges that extend from the spine, which is the upward erupting flux rope, to both sides. The slopes of the ridges indicate a propagation speeds on the order of 10^4 km/s. After $t = 275$ s, a few ridges (on the lower y side) exhibit downflows, which means that the atmosphere above may exert a downward push to that below this layer and those even deeper.

Similar behaviors were also reported by Afanasyev et al. (2023) and Fan et al. (2024). Unfortunately, their model may not have a setup that allows for studying the dynamics in the lower atmosphere. Therefore, we

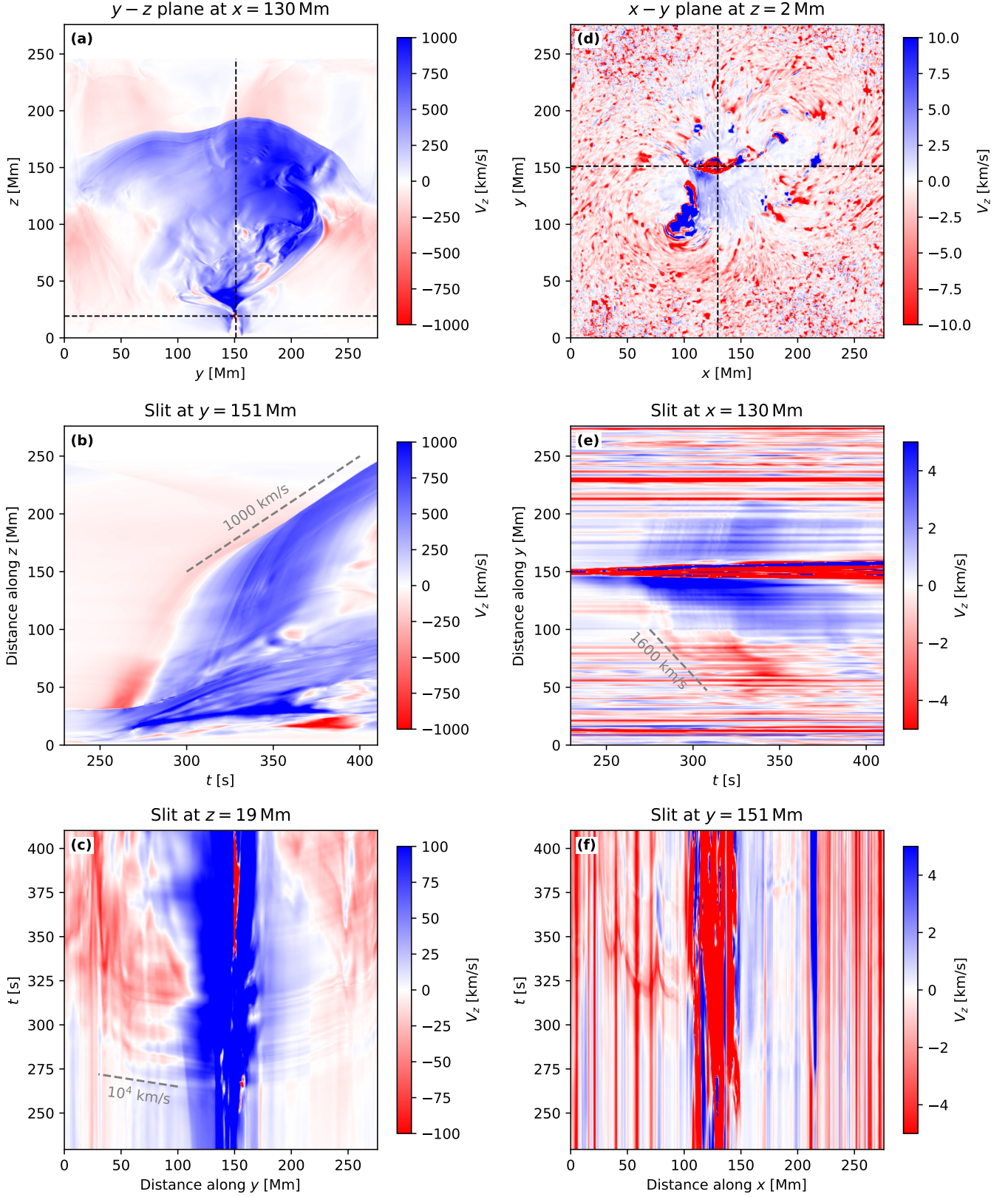


Figure 4. Piston-driven shock in the corona and the Moreton waves in the chromosphere. In the left column, Panel (a) presents the vertical velocity v_z at $t = 356$ s in a $y-z$ plane placed at $x = 130$ Mm; Panels (b) and (c) are time-distance diagrams of v_z along the vertical and horizontal slits, which are placed at the dashed lines in Panel (a), respectively. In the right column, Panel (d) shows v_z in a horizontal layer at 2 Mm height; Panels (e) and (f) are time-distance diagrams of v_z along the y - and x -slits, as indicated by the dashed lines in Panel (d), respectively.

examine this effect in our simulation in a deep horizontal layer at 2 Mm height in the chromosphere, as shown in Figure 4 (d). In the outer rim of the active region, which is dominated by downflows, a belt of slightly increased downward velocities (e.g., at $y = 60$ Mm) can be discerned. This disturbance is better revealed in Panel (e) by a time-distance diagram along the y -slit placed at the exact location of the $y - z$ plane. After $t = 275$ s, we see in this deep chromosphere layer a propagating downflow wave front to the south, which will generate a signal on the red-wing of chromospheric spectral lines such as how Moreton waves were discovered (Moreton & Ramsey 1960). The propagation speed of approximately 1600 km/s is surprisingly large compared with the typical sound speed in the chromosphere. It follows the long-known argument that such chromospheric waves cannot be sustained in the chromosphere but rather imprint the impact of waves/shocks propagating in the corona (Uchida 1968).

Panel (f) of Figure 4 displays a time-distance diagram along the x -slit marked by the horizontal dashed line in Panel (d). The imprint of coronal waves/shocks is only found to the east of the active region, and together with Figure 4 (e), it clearly demonstrates the asymmetric propagation of the Moreton wave.

3.4. Formation of Flare Ribbons

3.4.1. Plasma Dynamics in Flare Ribbons

Bright ribbons are the most prominent observational manifestations of solar flares in the lower atmosphere. The first row of Figure 5 displays the emission measures during the gradual phase in the domain below 12.8 Mm, where the contribution is mostly from the heated chromosphere and the lower legs of the post-flare loops. The emission measures over a broad temperature range are integrated into three bins. The brightest ribbons are found at the lower temperatures along the PIL. The flare ribbons at this moment have extended to the outer sunspots, N1 and P2, which are the footpoints of the large flux rope that is formed through reconnections during the eruption. The locations are consistent with the magnetic configuration shown in Figure 2.

Instead of the line-of-sight integrated velocity shown in Figure 3, we illustrate the plasma dynamics in flare ribbons via the velocity in at a constant temperature surface. Panels (d)–(f) reveal chromospheric evaporations and condensations in the flaring atmosphere in three layers through the field-aligned vertical velocity v_{bz} , which is given by

$$v_{bz} = (\mathbf{v} \cdot \mathbf{b}) b_z, \quad (4)$$

where $\mathbf{b} = \mathbf{B}/|\mathbf{B}|$ is the unit vector of the magnetic field. Moreover, the pressure gradient is the major driving force of field-aligned dynamics in response to energy deposition in the chromosphere. We present the pressure-driven vertical acceleration a_{pz} , which is evaluated by

$$a_{pz} = \frac{(\nabla p \cdot \mathbf{b}) b_z}{\rho}, \quad (5)$$

in the same temperature surfaces in Panels (g) – (i).

Strong downflows are found in temperatures over one MK at locations where the brightest ribbons are observed in the center of the active region and are cospatial with the strongest downward pressure gradient acceleration. Slightly weaker condensations are present in the extended ribbons. In the hottest surface, which corresponds to a slightly higher geometric height, the partition of upflows prevails, whereas are some points along the ribbon may still exhibit downflows. An extensive area off the flare ribbons is dominated by upflows from one MK. This is also consistent with the blue patches in Figure 5 (h), where the pressure gradient drives a very weak condensation at lower temperatures but evident evaporation at higher temperatures.

The dynamics observed in the simulation are attributed to the energy deposition in the chromosphere. In this simulation, conduction is the main agent that transports the magnetic energy that is released by reconnections in the corona down to the lower atmosphere. The bottom row of Figure 5 displays the thermal conduction flux in the three layers with increasing temperature (increasing height as well). A downward energy flux greater than 10^{11} erg/cm²/s is presents in the higher layers, which is comparable to the strongest energy injection rate assumed in radiative hydrodynamics calculations for solar flares (e.g., Allred et al. 2015; Reep et al. 2015; Kowalski et al. 2017), whereas the energy flux decays significantly with height and becomes the order of 10^9 erg/cm²/s at the surface of lower temperatures. This decay indicates a deposition of energy in this volume, particularly along the flare ribbons, where significant condensations and evaporations are driven by downward/upward pressure gradient forces.

We mark the locations of the sun-quake sources found by Kosovichev (2011) and Zharkov et al. (2011) during this flare in Panels (d) and (k). The observed sun-quake sources, which should be in a further deeper layer, are more or less cospatial with points of strong condensations, i.e., a high energy injection rate. Moreover, two of them appear to be the footpoints of the pre-existing flux rope along the central PIL, and the middle one is right beneath the reconnection site in the early stage of the flare, as illustrated in Figure 2. Although the present

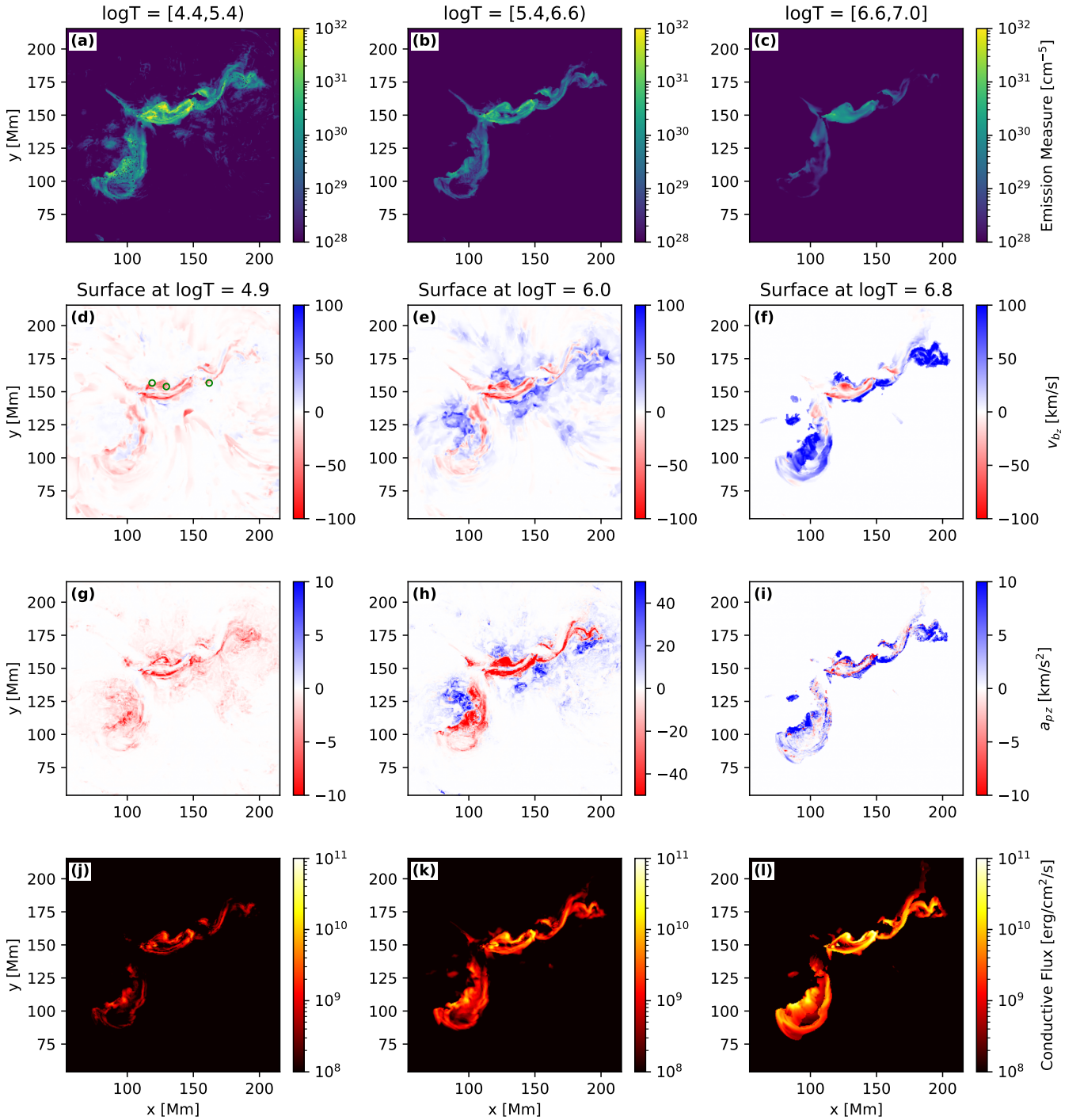


Figure 5. The flare ribbons at $t = 410$ s. Only the lowermost 12.8 Mm (200 grid points) are considered in this analysis to highlight the emission in the lowest part of the domain and to exclude the contribution from ejected chromospheric plasma with the erupted flux rope. The first row displays emission measures binned to three wide temperature ranges. The second row shows the vertical component of field-aligned velocities, i.e., the upward evaporation flows, at the surface of a certain temperature, as indicated above Panels (d)–(f). Panels (g)–(i) present the vertical acceleration driven by the pressure gradient force along the magnetic field. Panels (j)–(l) illustrate the thermal conduction flux at these three temperature surfaces.

model does not account for all the physics needed to model the trigger of the phenomenon, the comparison suggests a nontrivial similarity between the energy deposition site in the simulation and that in the real flare.

3.4.2. *Evolution of the flare ribbons and Coronal Magnetic Reconnection*

Finally, it is intriguing to examine the extent to which the flare ribbons in the model may resemble the observation of this flare and what is the magnetic configuration that directly causes the evolution of the ribbon. The AIA 1600Å channel images covering the change in the flare ribbons from the impulsive to the gradual phases are presented in the top row of Figure 6, which is compared with the total emission measure at all temperatures in the lower atmosphere, as shown in Figure 6 (e) – (h). The bottom row presents a top-down view of the magnetic field in a similar field of view.

In the impulsive phase shown in the first column in Figure 6, both the observation and simulation show bright ribbons along the central PIL and a brightening on the right side of the N2 spot. During the peak, while the brightest emission remains in the active region core, the ribbons extend to the center of the P1 spot, with bright patches above strong flux concentrations. The gradual phase in the third column demonstrates that the ribbons in both the observation and model start to fade and exhibit separating motion in the N–S direction. Finally, as time progresses, the two main ribbons become clearly more separated with significantly reduced brightness.

The magnetic field configuration reveals a crucial process in the early stage of the flare between the P3 flux concentration and the pre-existing flux rope along the PIL. As illustrated in Panel (i), part of the flux rope rooted at N1 is involved in a reconnection with the intruding P3 and is redirected to N2, resulting in the brightening observed on the right side of the N2 spot.

At the moment shown in Panel (j), reconnection between the larger arcades creates long hot loops rooted at the conjugate brightening in the two outer sunspots P1 and N2. Thus, the E–W extension of the ribbon is a manifestation of the continuous reconnections in the corona.

The latter two snapshots presented in Panels (k) and (l) illustrate, in closer view than those presented in Figure 2, the formation of a corridor of post-flare loops. As the large flux rope rises and triggers reconnection between the large scale envelope field, as shown in Figure 2 (g), longer and higher loops with apparently weak shear form, whose footpoints map the expanded flare ribbon seen in the emission features.

4. SUMMARY AND DISCUSSION

In this paper, we present the application of the data-driven branch of the MURaM code to a well-known flare-productive active region. The key results are summarized as follows.

The complete three-stage model demonstrates the emergence of the magnetic field from the photosphere to the corona and a major solar eruption that releases 10^{32} erg magnetic energy and yields a soft X-ray flux on a similar order of magnitude as the real event. In the large-scale atmosphere, the eruption drives bulk mass ejections and a dome-like shock front; meanwhile, the coronal eruption deliver a sufficiently strong impact to the outer rim of the active region that penetrates until the chromosphere and creates a fast-propagating Moreton wave. The released magnetic energy is deposited in the chromosphere by strong downward conduction fluxes that are greater than 10^{11} erg/cm²/s. Local pressure peaks drive chromospheric condensation and evaporation. The temporal evolution of the bright flare ribbons in the simulation, which maps the development of reconnections in the coronal magnetic field, is consistent with the observation of this flare.

Observations have suggested that the seminal structure of this eruption was a flux rope along the highly sheared PIL between the N2 and P1 spots. Despite of the different magnetic initial conditions and boundary driving methods, data-driven simulations of AR 11158 have consistently reproduced such a magnetic structure (Inoue et al. 2014; Hayashi et al. 2018; Afanasyev et al. 2023; Fan et al. 2024). In our model, we use a simple approach of Cheung & DeRosa (2012). Although the outer part of the active region exhibits some artificial twist at the large scale due to the constant Ω and horizontal size boundary, the choice of $\Omega = 1.0 \times 10^{-1} \text{ s}^{-1}$ is able to build an appropriate flux rope that creates an eruption of a similar strength as the real flare.

The plasma dynamics in flare loops have been thoroughly investigated in classical hydrodynamics calculations (Fisher et al. 1985). Idealized 3D MHD models suggest that the location of the flare ribbons reflect the cross sections of magnetic separatrixes in the lower atmosphere (e.g., Janvier et al. 2014; Savcheva et al. 2015). The ingredients of these models must be combined in 3D radiative MHD simulations to yield flare ribbons that can be compared with observations, as performed by Cheung et al. (2019) in an MURaM simulation inspired by observations.

Furthermore, reproducing the observed ribbons in this particular flare is more challenging. Inoue et al. (2014) used magnetic properties to project the location of flare ribbons in the model, which appeared to be similar

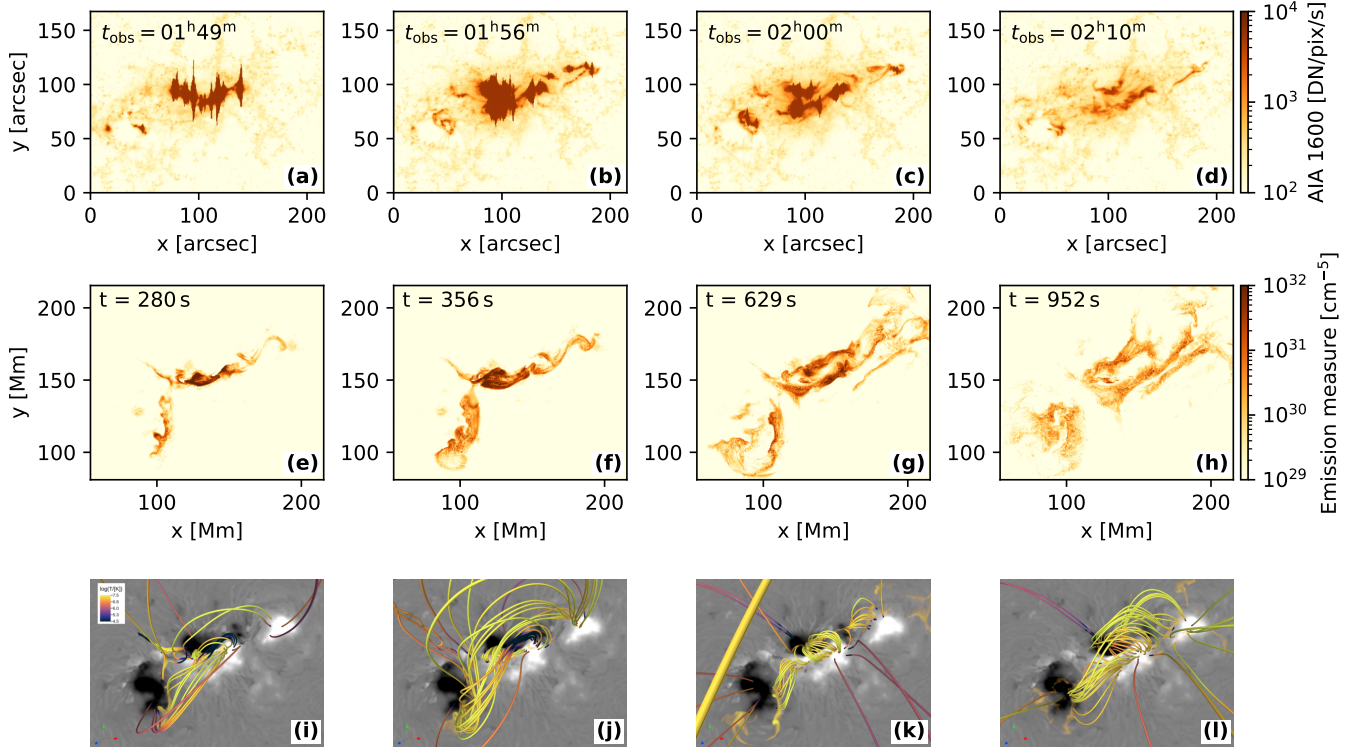


Figure 6. Comparison of the flare ribbons in the observation and simulation. The top row displays the evolution of flare ribbons captured by the AIA 1600 channel. The middle row shows the flare ribbon in the simulation, which is manifested by the emission measure in the lowermost 200 grid points at all temperatures. The bottom row illustrates magnetic field lines that are closely related to flare ribbons. The grayscale images are B_z in the photosphere of the simulation, overlaid by a horizontal slice at 2.5 Mm height showing plasma temperatures, as indicated by the color table. Only temperatures higher than 10 MK are displayed, whereas lower values are transparent. Two groups of magnetic field lines are displayed: one group is calculated from seed points that are randomly distributed in regions with bright ribbons with a bias to high density and the other group has a bias to high temperature. The color of the fieldlines represents the plasma temperature, as indicated by the same color table of the slice.

to the observed ribbons. The models presented by Afanasyev et al. (2023) and Fan et al. (2024) stand for the state-of-art of data-driven models of this active region thus far in the literature. The former illustrated the location of flare ribbons by a temperature proxy instead of a direction observable, because of some missing ingredients in the coronal energy balance. The latter improved the energy equation; however, unfortunately, the bottom boundary has a fixed chromospheric temperature and density, which limited investigations of flare ribbons and the chromospheric impact of the coronal shock. Therefore, to the best of our knowledge, the work presented in this paper may be the first model that self-consistently describes the evolution of flare ribbons, which resembles a real flare in a one-to-one fashion.

In addition to studying this particular active region, which has been performed rather thoroughly, the simulations presented in this paper could also be useful for investigating, in general, the gradual evolution of a flux rope before the eruption and the trigger of the onset.

The data-driven MURaM code can be of cause applied in general to other observed active regions, as long as a time series of the vertical magnetic field is available. It is also interesting to test in the further how our simulations perform when they are driven by the electric field used in other models Kazachenko et al. (2014); Fisher et al. (2020) or a more sophisticated characteristic boundary developed by Tarr et al. (2024).

ACKNOWLEDGMENTS

F.C. is supported by National Science Foundation of China No. 12422308 and No. 12373054, and by the National Key R&D Program of China under grant 2021YFA1600504. This work benefits from discussions during the ISSI workgroup “Data-driven 3D Modeling of Evolving and Eruptive Solar Active Region Corone”. The visualization shown in Figures 1, 2, and 6 are created by VAPOR (Li et al. 2019).

AUTHOR CONTRIBUTIONS

F.C. conducted the numerical simulations, performed the analysis and visualization, and wrote the texts.

REFERENCES

- Afanasyev, A. N., Fan, Y., Kazachenko, M. D., & Cheung, M. C. M. 2023, *ApJ*, 952, 136, doi: [10.3847/1538-4357/acd7e9](https://doi.org/10.3847/1538-4357/acd7e9)
- Allred, J. C., Kowalski, A. F., & Carlsson, M. 2015, *ApJ*, 809, 104, doi: [10.1088/0004-637X/809/1/104](https://doi.org/10.1088/0004-637X/809/1/104)
- Aschwanden, M. J., Holman, G., O’Flannagain, A., et al. 2016, *ApJ*, 832, 27, doi: [10.3847/0004-637X/832/1/27](https://doi.org/10.3847/0004-637X/832/1/27)
- Chen, F. 2025, arXiv e-prints, arXiv:2511.02362, doi: [10.48550/arXiv.2511.02362](https://doi.org/10.48550/arXiv.2511.02362)
- Chen, F., Cheung, M. C. M., Rempel, M., & Chintzoglou, G. 2023a, *ApJ*, 949, 118, doi: [10.3847/1538-4357/acc8c5](https://doi.org/10.3847/1538-4357/acc8c5)
- Chen, F., Rempel, M., & Fan, Y. 2022, *ApJ*, 937, 91, doi: [10.3847/1538-4357/ac8f95](https://doi.org/10.3847/1538-4357/ac8f95)
- . 2023b, *ApJL*, 950, L3, doi: [10.3847/2041-8213/acda2e](https://doi.org/10.3847/2041-8213/acda2e)
- Cheng, X., Zhang, J., Kliem, B., et al. 2020, *ApJ*, 894, 85, doi: [10.3847/1538-4357/ab886a](https://doi.org/10.3847/1538-4357/ab886a)
- Cheung, M. C. M., & DeRosa, M. L. 2012, *ApJ*, 757, 147, doi: [10.1088/0004-637X/757/2/147](https://doi.org/10.1088/0004-637X/757/2/147)
- Cheung, M. C. M., Rempel, M., Chintzoglou, G., et al. 2019, *Nature Astronomy*, 3, 160, doi: [10.1038/s41550-018-0629-3](https://doi.org/10.1038/s41550-018-0629-3)
- Chintzoglou, G., Zhang, J., Cheung, M. C. M., & Kazachenko, M. 2019, *ApJ*, 871, 67, doi: [10.3847/1538-4357/aaef30](https://doi.org/10.3847/1538-4357/aaef30)
- Dissauer, K., Veronig, A. M., Temmer, M., Podladchikova, T., & Vanninathan, K. 2018, *ApJ*, 855, 137, doi: [10.3847/1538-4357/aaadb5](https://doi.org/10.3847/1538-4357/aaadb5)
- Fan, Y., Kazachenko, M. D., Afanasyev, A. N., & Fisher, G. H. 2024, *ApJ*, 975, 206, doi: [10.3847/1538-4357/ad7f53](https://doi.org/10.3847/1538-4357/ad7f53)
- Fisher, G. H., Canfield, R. C., & McClymont, A. N. 1985, *ApJ*, 289, 414, doi: [10.1086/162901](https://doi.org/10.1086/162901)
- Fisher, G. H., Kazachenko, M. D., Welsch, B. T., et al. 2020, *ApJS*, 248, 2, doi: [10.3847/1538-4365/ab8303](https://doi.org/10.3847/1538-4365/ab8303)
- Guo, Y., Guo, J., Ni, Y., et al. 2024, *Reviews of Modern Plasma Physics*, 8, 29, doi: [10.1007/s41614-024-00167-2](https://doi.org/10.1007/s41614-024-00167-2)
- Hayashi, K., Feng, X., Xiong, M., & Jiang, C. 2018, *ApJ*, 855, 11, doi: [10.3847/1538-4357/aaacd8](https://doi.org/10.3847/1538-4357/aaacd8)
- . 2019, *ApJL*, 871, L28, doi: [10.3847/2041-8213/aaffcf](https://doi.org/10.3847/2041-8213/aaffcf)
- Hoeksema, J. T., Liu, Y., Hayashi, K., et al. 2014, *SoPh*, 289, 3483, doi: [10.1007/s11207-014-0516-8](https://doi.org/10.1007/s11207-014-0516-8)
- Hoeksema, J. T., Abbett, W. P., Bercik, D. J., et al. 2020, *ApJS*, 250, 28, doi: [10.3847/1538-4365/abb3fb](https://doi.org/10.3847/1538-4365/abb3fb)
- Inoue, S., Hayashi, K., Magara, T., Choe, G. S., & Park, Y. D. 2014, *ApJ*, 788, 182, doi: [10.1088/0004-637X/788/2/182](https://doi.org/10.1088/0004-637X/788/2/182)
- . 2015, *ApJ*, 803, 73, doi: [10.1088/0004-637X/803/2/73](https://doi.org/10.1088/0004-637X/803/2/73)
- Inoue, S., Kusano, K., Büchner, J., & Skála, J. 2018, *Nature Communications*, 9, 174, doi: [10.1038/s41467-017-02616-8](https://doi.org/10.1038/s41467-017-02616-8)
- Janvier, M., Aulanier, G., Bommier, V., et al. 2014, *ApJ*, 788, 60, doi: [10.1088/0004-637X/788/1/6010.48550/arXiv.1402.2010](https://doi.org/10.1088/0004-637X/788/1/6010.48550/arXiv.1402.2010)
- Jarolim, R., Thalmann, J. K., Veronig, A. M., & Podladchikova, T. 2023, *Nature Astronomy*, 7, 1171, doi: [10.1038/s41550-023-02030-9](https://doi.org/10.1038/s41550-023-02030-9)
- Jiang, C. 2024, *Science China Earth Sciences*, 67, 3765, doi: [10.1007/s11430-023-1402-3](https://doi.org/10.1007/s11430-023-1402-3)
- Jiang, C., Feng, X., Guo, Y., & Hu, Q. 2022, *The Innovation*, 3, 100236, doi: [10.1016/j.xinn.2022.100236](https://doi.org/10.1016/j.xinn.2022.100236)
- Jiang, C., Feng, X., Liu, R., et al. 2021, *Nature Astronomy*, 5, 1126, doi: [10.1038/s41550-021-01414-z](https://doi.org/10.1038/s41550-021-01414-z)
- Jin, M., Cheung, M. C. M., DeRosa, M. L., Nitta, N. V., & Schrijver, C. J. 2022, *ApJ*, 928, 154, doi: [10.3847/1538-4357/ac589b](https://doi.org/10.3847/1538-4357/ac589b)
- Kazachenko, M. D., Fisher, G. H., & Welsch, B. T. 2014, *ApJ*, 795, 17, doi: [10.1088/0004-637X/795/1/17](https://doi.org/10.1088/0004-637X/795/1/17)
- Kazachenko, M. D., Fisher, G. H., Welsch, B. T., Liu, Y., & Sun, X. 2015, *ApJ*, 811, 16, doi: [10.1088/0004-637X/811/1/16](https://doi.org/10.1088/0004-637X/811/1/16)
- Kosovichev, A. G. 2011, *ApJL*, 734, L15, doi: [10.1088/2041-8205/734/1/L15](https://doi.org/10.1088/2041-8205/734/1/L15)
- Kowalski, A. F., Allred, J. C., Daw, A., Cauzzi, G., & Carlsson, M. 2017, *ApJ*, 836, 12, doi: [10.3847/1538-4357/836/1/12](https://doi.org/10.3847/1538-4357/836/1/12)
- Li, S., Jaroszynski, S., Pearse, S., Orf, L., & Clyne, J. 2019, *Atmosphere*, 10, doi: [10.3390/atmos10090488](https://doi.org/10.3390/atmos10090488)
- Liu, Y., & Schuck, P. W. 2012, *ApJ*, 761, 105, doi: [10.1088/0004-637X/761/2/105](https://doi.org/10.1088/0004-637X/761/2/105)
- Lumme, E., Pomoell, J., & Kilpua, E. K. J. 2017, *SoPh*, 292, 191, doi: [10.1007/s11207-017-1214-0](https://doi.org/10.1007/s11207-017-1214-0)
- Milligan, R. O., Kerr, G. S., Dennis, B. R., et al. 2014, *ApJ*, 793, 70, doi: [10.1088/0004-637X/793/2/70](https://doi.org/10.1088/0004-637X/793/2/70)
- Moreton, G. E., & Ramsey, H. E. 1960, *PASP*, 72, 357, doi: [10.1086/127549](https://doi.org/10.1086/127549)

- Patsourakos, S., Vourlidas, A., Török, T., et al. 2020, *SSRv*, 216, 131, doi: [10.1007/s11214-020-00757-9](https://doi.org/10.1007/s11214-020-00757-9)
- Reep, J. W., Bradshaw, S. J., & Alexander, D. 2015, *ApJ*, 808, 177, doi: [10.1088/0004-637X/808/2/177](https://doi.org/10.1088/0004-637X/808/2/177)
- Rempel, M., Chintzoglou, G., Cheung, M. C. M., Fan, Y., & Kleint, L. 2023, *ApJ*, 955, 105, doi: [10.3847/1538-4357/aced4d](https://doi.org/10.3847/1538-4357/aced4d)
- Savcheva, A., Pariat, E., McKillop, S., et al. 2015, *ApJ*, 810, 96, doi: [10.1088/0004-637X/810/2/96](https://doi.org/10.1088/0004-637X/810/2/96)
- Scherrer, P. H., Schou, J., Bush, R. I., et al. 2012, *SoPh*, 275, 207, doi: [10.1007/s11207-011-9834-2](https://doi.org/10.1007/s11207-011-9834-2)
- Schmieder, B., Guo, J., & Poedts, S. 2024, *Reviews of Modern Plasma Physics*, 8, 27, doi: [10.1007/s41614-024-00166-3](https://doi.org/10.1007/s41614-024-00166-3)
- Schrijver, C. J., Aulanier, G., Title, A. M., Pariat, E., & Delannée, C. 2011, *ApJ*, 738, 167, doi: [10.1088/0004-637X/738/2/167](https://doi.org/10.1088/0004-637X/738/2/167)
- Sun, X., Hoeksema, J. T., Liu, Y., Kazachenko, M., & Chen, R. 2017, *ApJ*, 839, 67, doi: [10.3847/1538-4357/aa69c1](https://doi.org/10.3847/1538-4357/aa69c1)
- Sun, X., Hoeksema, J. T., Liu, Y., et al. 2012, *ApJ*, 748, 77, doi: [10.1088/0004-637X/748/2/77](https://doi.org/10.1088/0004-637X/748/2/77)
- Tarr, L. A., Kee, N. D., Linton, M. G., Schuck, P. W., & Leake, J. E. 2024, *ApJS*, 270, 30, doi: [10.3847/1538-4365/ad0e0c](https://doi.org/10.3847/1538-4365/ad0e0c)
- Toriumi, S., Schrijver, C. J., Harra, L. K., Hudson, H., & Nagashima, K. 2017, *ApJ*, 834, 56, doi: [10.3847/1538-4357/834/1/56](https://doi.org/10.3847/1538-4357/834/1/56)
- Tziotziou, K., Georgoulis, M. K., & Liu, Y. 2013, *ApJ*, 772, 115, doi: [10.1088/0004-637X/772/2/115](https://doi.org/10.1088/0004-637X/772/2/115)
- Uchida, Y. 1968, *SoPh*, 4, 30, doi: [10.1007/BF00146996](https://doi.org/10.1007/BF00146996)
- Vemareddy, P., Ambastha, A., & Maurya, R. A. 2012, *ApJ*, 761, 60, doi: [10.1088/0004-637X/761/1/60](https://doi.org/10.1088/0004-637X/761/1/60)
- Wang, C., Chen, F., Ding, M., & Lu, Z. 2023, *ApJ*, 956, 106, doi: [10.3847/1538-4357/acedfe](https://doi.org/10.3847/1538-4357/acedfe)
- Wang, S., Liu, C., Liu, R., et al. 2012, *ApJL*, 745, L17, doi: [10.1088/2041-8205/745/2/L17](https://doi.org/10.1088/2041-8205/745/2/L17)
- Warmuth, A., & Mann, G. 2016, *A&A*, 588, A116, doi: [10.1051/0004-6361/201527475](https://doi.org/10.1051/0004-6361/201527475)
- Young, P. R., Doschek, G. A., Warren, H. P., & Hara, H. 2013, *ApJ*, 766, 127, doi: [10.1088/0004-637X/766/2/127](https://doi.org/10.1088/0004-637X/766/2/127)
- Zharkov, S., Green, L. M., Matthews, S. A., & Zharkova, V. V. 2011, *ApJL*, 741, L35, doi: [10.1088/2041-8205/741/2/L35](https://doi.org/10.1088/2041-8205/741/2/L35)